

Comparison of different one-parameter damage laws and local stress-strain approaches in multiaxial fatigue life assessment of notched components

R. Branco^{a1}, J.D. Costa^a, L.P. Borrego^{b,a}, F. Berto^c, S.M.J. Razavi^c, W. Macek^d

^a University of Coimbra, CEMMPRE, Department of Mechanical Engineering, Coimbra, Portugal

^b Department of Mechanical Engineering, Coimbra Polytechnic - ISEC, Rua Pedro Nunes, Quinta da Nora, 3030-199 Coimbra, Portugal

^c Department of Mechanical and Industrial Engineering, NTNU, 7491 Trondheim, Norway

^d Opole University of Technology, Prószkowska 76, 45-758 Opole, Poland

Highlights

- Different local stress-strain approaches in multiaxial notch fatigue are compared
- Cyclic plasticity at the notch root is accounted for using linear-elastic stresses
- Multiaxial fatigue life better estimated using energy-based models

Abstract

This paper aims to compare the predictive capabilities of different one-parameter damage laws and local stress-strain approaches to assess the fatigue lifetime in notched components subjected to proportional bending-torsion loading. The tested fatigue damage parameters are defined using well-known stress-based, strain-based, SWT-based and energy-based relationships. Multiaxial cyclic plasticity at the notch-controlled process zone is accounted for within a 3D-FE linear-elastic framework using three local stress-strain approaches, namely Neuber's rule, equivalent strain energy density rule (ESED) and the modified ESED rule. Regarding the local stress-strain approaches, irrespective of the fatigue damage parameter, Neuber's rule always led to more conservative results, and the modified ESED rule resulted in slightly better fatigue life predictions when compared to the original ESED rule. As far as the fatigue damage parameters are concerned, energy-based models were more accurate, irrespective of the local stress-strain approach.

¹ Corresponding author: ricardo.branco@dem.uc.pt (R. Branco)

Keywords: multiaxial fatigue; notch effect; cyclic plasticity; Neuber's rule; equivalent strain energy density

1. Introduction

Fatigue life assessment of mechanical components experiencing multiaxial loading is a complex challenge. In part, this is because there is a myriad of variables involved in the analysis, namely the shape of the stress raiser, the normal stresses to shear stresses ratio, the loading orientation with respect to the notch configuration, among others [1-3]. The unlimited number of possibilities associated with the above-mentioned variables increases the difficulty and introduces some degree of unpredictability. Thus, there is a need for unified models capable of accounting for the fatigue damage at the critical points in an accurate manner [4-5].

The development of a universal multiaxial fatigue model remains an important goal for the scientific community. Nevertheless, despite the long debate over the last decades, there is no consensus regarding a unique criterion. Within the most successful approaches to assess the multiaxial fatigue lifetime, there are many criteria grounded on the idea of reducing the multiaxial state to an equivalent uniaxial state [6-8]. In this line of thought, a representative fatigue damage parameter, which can be expressed in terms of stress-based, strain-based, or energy-based relationships, is determined and then compared to the uniaxial fatigue response of the material to estimate the life expectancy [9-10].

Different approaches can be engineered to define a representative fatigue damage quantifier. It can be defined simply by an average parameter estimated at a specific distance from the notch tip, or by using more sophisticated approaches, namely weighted methods [11-12]. The Theory of Critical Distances is one of the most popular average stress methods [13]. Its proliferation has been associated with the balance between simplicity and accuracy. Another very popular group of methods formalised using energy considerations are those based on the Strain Energy Density concept [14-19]. The possibility to deal with a large variety of problems and loading scenarios makes them very attractive [20].

Regarding the cyclic plasticity response at the notch root, the current strategies are usually materialised by means of experimental techniques, numerical methods, or approximate solutions [21]. Experimental techniques, due to their intrinsic nature, have some limitations, such as the difficulty to assess complicated geometric details or the impossibility to evaluate

the stress-strain fields inside the body [12]. With the advent of computer technology, numerical methods have been a strong ally in the analysis of complex geometries, providing precise results not only at the surface, but also in depth.

As far as the numerical methods are concerned, local stress-strain histories are generally computed considering elastic-plastic simulations or pseudo-elastic analyses [12,22]. Although, in theory, the former are more precise, the latter have the advantage of being faster and simpler, because they do not require complex constitutive models, nor too much computational time, while providing high efficiency. In this ambit, we mention the so-called Neuber's rule, the equivalent strain energy density rule, and the modified strain energy density rule [23-25]. Previous research focused on the accuracy of the two first techniques has reported that the ESED rule tends to underestimate the notch root strains, while the other tends to overestimate them [21]. The modified ESED rule is believed to be closer to the real stress-strain histories [12,25].

This paper aims to investigate the accuracy of various multiaxial fatigue models for notched components, developed by the combination of different well-known one-parameter damage laws and local stress-strain approaches. To the best of our knowledge, there are no systematic studies dealing with this subject. In the beginning, we briefly address the basic concepts of the tested models and the main governing equations. Then, the experimental fatigue program and the simulation details are described. Further, we estimate the fatigue lifetime for each multiaxial model and compare the predictive capabilities based on a statistical evaluation. The paper ends with some concluding remarks.

2. Fatigue life assessment models

The fatigue life assessment models considered in this research aim at comparing the predictive capabilities of different uniaxial one-parameter damage laws and local stress-strain approaches defined from pseudo-elastic stress-strain fields. The employed procedure is schematically shown in Figure 1. The modus operandi, presented in Figure 1, consists of four main steps:

- (1) reduction of the multiaxial stress-strain state to an equivalent uniaxial stress-strain state based on the von Mises stress (Figure 1(a));

- (2) definition of an average stress range at the notch-controlled process zone using the Line Method of the Theory of Critical Distances (TCD) (Figure 1(b));
- (3) generation of a uniaxial stress-strain hysteresis loop representative of the loading case via a local pseudo-elastic stress-strain approach (Figure 1(c));
- (4) determination of fatigue lifetime by inserting the associated value of the damage parameter into a uniaxial one-parameter damage law (Figure 1(d)).

In this analysis, it is assumed that the fatigue lifetime needed to initiate a macro-crack in a notched component or a smooth specimen is the same if the local stress-strain behaviour at the notch-controlled zone is similar in both the notched component and the smooth specimen. The next sections present the background of the models, namely the Line Method of TCD as well as the local stress-strain approaches and the one-parameter damage laws considered in the paper.

2.1 Theory of Critical Distances

The Theory of Critical Distances (TCD), a unifying theory introduced by Taylor, represents a group of average stress methods which are based on the idea that fatigue failure takes place if a critical volume of the material at the notch component is subjected to a critical stress [11,13]. The TCD gathers four main methods, more specifically the Point Method, Line Method, Area Method, and Volume Method [11,13].

Here, for the sake of clarity, only the Line Method is addressed. First proposed by Neuber, as schematised in Figure 1(b), this method postulates that the effective stress range ($\Delta\sigma_{\text{eff}}$) is determined along a straight line emanating from the notch bisector over a distance equal to $2a_0$, i.e.

$$\Delta\sigma_{\text{eff}} = \frac{1}{2a_0} \int_0^{2a_0} \Delta\sigma(r) dr \quad \text{Eq. (1)}$$

where a_0 represents the material characteristic length which can be defined as follows:

$$a_0 = \frac{1}{\pi} \left(\frac{\Delta K_{\text{th}}}{\Delta\sigma_0} \right)^2 \quad \text{Eq. (2)}$$



being ΔK_{th} the threshold value of the stress intensity factor range, and $\Delta\sigma_0$ the material plain fatigue limit. The two-above mentioned variables are determined under the same stress ratio of the notched component. More details about the Theory of Critical Distances can be found in the recent papers published by Taylor [13,23].

2.2 Local stress-strain approaches

Within the current methods to deal with the notch plasticity effect, numerical approaches have been successfully used. Among other reasons, the possibility to extract precise information, not only at the notch surface, but also inside the body, make them extremely advantageous. In addition, with the advent of computer technology and the development of advanced numerical methods, pseudo-elastic approaches are particularly attractive, because of their simplicity of implementation, speed of simulation, and high efficiency [12]. In this paper, we implement and compare three well-established approaches, namely the Neuber's rule, the equivalent strain energy density rule, and the modified equivalent strain energy density rule [24-26].

The so-called Neuber's rule, which was initially derived from the analysis of prismatic bodies with hyperbolic notches subjected to monotonic shear loading, states that the geometric mean value of both the stress concentration factor and the strain concentration factor is constant at any load state and equals the elastic stress concentration factor [24]. Under monotonic loading (see Figure 1(c)), it leads to:

$$\sigma^2 + E \sigma \left(\frac{\sigma}{k}\right)^{\frac{1}{n}} = k_t^2 S^2 \quad \text{Eq. (3)}$$

and under cyclic loading (see Figure 1(c)), we may write:

$$\Delta\sigma^2 + 2 E \Delta\sigma \left(\frac{\sigma}{k'}\right)^{\frac{1}{n'}} = k_t^2 \Delta S^2 \quad \text{Eq. (4)}$$

where n and n' are the strain hardening coefficient and the cyclic strain hardening coefficient, k and k' are the strain hardening exponent and the cyclic strain hardening exponent, k_t is the stress concentration factor, E is the Young's modulus, S and ΔS are the nominal stress and the nominal stress range, and σ and $\Delta\sigma$ are the local stress and the local stress range.

Proposed by Molski and Glinka [25], the equivalent strain energy density (ESED) rule is an alternative approach to deal with local stress-strain history. The main hypothesis behind this concept is that the elastic-plastic strain energy density of the material in the yielded zone is theoretically the same as the pseudo-strain energy assuming the material is in an elastic state. Under monotonic loading, it results as:

$$\frac{\sigma^2}{E} + \frac{2\sigma}{n+1} \left(\frac{\sigma}{k}\right)^{\frac{1}{n}} = \frac{k_t^2 S^2}{E} \quad \text{Eq. (5)}$$

and under cyclic loading, we may use Eq. (6).

$$\frac{\Delta\sigma^2}{4E} + \frac{\Delta\sigma}{n'+1} \left(\frac{\Delta\sigma}{2k'}\right)^{\frac{1}{n'}} = \frac{k_t^2 \Delta S^2}{4E} \quad \text{Eq. (6)}$$

Ye et al. [23] have found a physical relationship between the two above-mentioned methods. Neuber's rule can be interpreted as a particular case of the ESED rule, i.e. it corresponds to the special cases in which the energy dissipated during the plastic deformation process at the notch region can be ignored. Based on the real physical stress-strain behaviour at the notch root, these researchers proposed a modified version of the ESED rule, which assumes that both the local stresses and the local strains are associated with the stored energy and that heat energy is considered as the dissipation [23]. Under monotonic loading, it leads to:

$$\frac{\sigma^2}{E} + \frac{(2-n)\sigma}{n+1} \left(\frac{\sigma}{k}\right)^{\frac{1}{n}} = \frac{k_t^2 S^2}{E} \quad \text{Eq. (7)}$$

and under cyclic loading, we may obtain Eq. (8).

$$\frac{\Delta\sigma^2}{4E} + \frac{(2-n')\Delta\sigma}{2(n'+1)} \left(\frac{\Delta\sigma}{2k'}\right)^{\frac{1}{n'}} = \frac{k_t^2 \Delta S^2}{4E} \quad \text{Eq. (8)}$$

2.3 One-parameter damage laws

From an engineering point of view, the life to initiate a macro-crack in a one-parameter damage representation, assumed here as the fatigue life criterion, can be defined as follows [27]:



$$\psi = f(2N_f) \quad \text{Eq. (9)}$$

where ψ is the fatigue damage parameter and $2N_f$ is the number of reversals to failure, or in a broader sense, the fatigue lifetime. This relationship, represented on a log-log scale by the full line of Figure 1(d), can be written in the form:

$$\psi = \kappa(2N_f)^\alpha + \psi_0 \quad \text{Eq. (10)}$$

here κ and α are material constants, $2N_f$ is the number of reversals to failure, and ψ_0 is the fatigue limit. In the cases where the fatigue limit does not exist, setting $\psi_0 = 0$, the previous equation leads to the following formula:

$$\psi = \kappa(2N_f)^\alpha \quad \text{Eq. (11)}$$

which is plotted in Figure 1(d) by the dashed straight line. In this study, as referred to above, we consider different well-known uniaxial fatigue damage parameters defined using stress-based, strain-based, and energy-based phenomenological laws. The selected parameters are briefly addressed below.

Stress-based approaches were the first attempts to study the fatigue phenomenon in a systematic approach. Based on the Basquin's relation, and the correction introduced by Morrow to account for the mean stress effect, the stress amplitude (σ_a) can be defined as the damage parameter. Thus, the correlation between σ_a and the fatigue life ($2N_f$) can be written as follows:

$$\sigma_a = (\sigma'_f - \sigma_m) (2N_f)^b \quad \text{Eq. (12)}$$

where σ'_f is the fatigue strength coefficient, b is the fatigue strength exponent, and σ_m is the mean stress.

Strain-based relationships are alternative approaches to evaluate the fatigue lifetime. Here, it is considered the Coffin-Manson model, whose fatigue damage parameter is the total strain

amplitude (ε_a). Introducing the correction of the elastic term proposed by Morrow to account for the mean stress effect, we get the following equation [28-30]:

$$\varepsilon_a = \frac{(\sigma'_f - \sigma_m)}{E} (2N_f)^b + \varepsilon'_f (2N_f)^c \quad \text{Eq. (13)}$$

where σ'_f is the fatigue strength coefficient, σ_m is the mean stress, b is the fatigue strength exponent, ε'_f is the fatigue ductility coefficient, c is the fatigue strength exponent, and E is Young's modulus.

Energy-based approaches assume that strain energy dissipated per cycle is the main contributor to the fatigue damage process. In this study, we consider the total strain energy density (ΔW_t) which has the ability to unify both the low-cycle and the high-cycle fatigue regimes and is capable of accounting for the mean stress effect [24]. The relationship between ΔW_t and the fatigue life ($2N_f$) can be established via the following formula [31]:

$$\Delta W_t = \kappa_t (2N_f)^{\alpha_t} + \Delta W_{0t} \quad \text{Eq. (14)}$$

where κ_t and α_t are material constants, and ΔW_{0t} is the tensile elastic energy at the material fatigue limit.

The Smith-Watson-Topper (SWT) damage parameter [32], which also has an energy-based nature, is another very popular approach to account for the mean stress effect [33]. It is defined by the product of maximum stress (σ_{max}) and the strain amplitude (ε_a), i.e.

$$\varepsilon_a \sigma_{max} = \frac{(\sigma'_f)^2}{E} (2N_f)^{2b} + \sigma'_f \varepsilon'_f (2N_f)^{b+c} \quad \text{Eq. (15)}$$

where σ'_f is the fatigue strength coefficient, b is the fatigue strength exponent, ε'_f is the fatigue ductility coefficient, c is the fatigue strength exponent, and E is Young's modulus.



3. Material and methods

3.1 Material

The material of this study is the 34CrNiMo6 high-strength steel, supplied in the form of a 20mm-diameter round bar. Its chemical composition and its main mechanical properties for the quenched and tempered (Q&T) grade are presented in Table 1 and Table 2, respectively. Both the cyclic strain hardening coefficient and the cyclic strain hardening exponent were obtained under fully-reversed strain-control mode [34], while the fatigue stress range ($\Delta\sigma_0$) and the stress intensity factor range threshold (ΔK_{th0}) were determined for pulsating loading conditions under stress-control and load-control modes, respectively [35].

3.2 Low-cycle fatigue tests

Low-cycle fatigue tests were performed in strain-control mode, according to ASTM E606-19 standard, using symmetrical loading scenarios ($R_\epsilon = -1$) and a constant strain rate ($d\epsilon/dt = 8 \times 10^{-3}$ s) with strain amplitudes in the interval 0.5-2.0% [35]. The specimen geometry (see Figure 2(a)) had a cylindrical gauge section with a length of 15 mm and a diameter of 8 mm. Data were acquired using an extensometer with a gauge length of 12.5 mm connected directly to the specimen. Tests were interrupted when the specimens reached the total failure. Table 3 presents a brief overview of the loading cases tested in this research and the main variables registered for the half-life cycle.

3.3 Multiaxial fatigue tests

Multiaxial fatigue tests were done using cylindrical specimens with a lateral U-shaped notch (see Figure 2(b)), under in-phase constant-amplitude pulsating loading conditions, assuming two ratios of the bending moment to the torsion moment (B/T), i.e. $B/T=2$ and $B/T=1$; and three orientations (θ) of the bending moment with respect to the notch root, i.e. $\theta=0^\circ$, 45° and 90° [36]. For each loading case, at least three nominal normal stress amplitudes (σ_a) were applied. The notch root was monitored in-situ using a high-resolution digital camera to detect the crack initiation sites and to track the crack paths. The number of cycles to fatigue crack initiation (N_i) was calculated for a crack length equal to a_0 (see Eq. (2)). A summary of the loading scenarios and nominal stress levels applied in the tests is exhibited in Table 4. More details about these tests can be found in a former paper of the authors [35,36].

3.4 Numerical modelling and simulation

The evaluation of the stress and strain fields at the notch root was carried out using a three-dimensional finite element model representative of the experimental tests. The assembled model, displayed in Figure 3, assumed a homogeneous, linear-elastic, and isotropic material, and was created in a parametric manner with 8-node hexahedral elements. At the notch region, an ultra-dense mesh was introduced in order to better characterise the stress-strain gradients. The final mesh density (76,608 elements and 99,823 nodes) was obtained through a careful optimisation study, in a step-wise manner, by increasing the number of finite elements, based on the principle that the stress field tends to stabilise with mesh refinement. Bending moments and torsion moments were generated by two pairs of forces (F_B and F_T , respectively) applied at one end of the specimen, while the other end was fixed.

4. Results and discussion

This section is organised into three sub-sections. Firstly, we analyse the cyclic stress-strain response of the tested material under uniaxial low-cycle fatigue loading and compute the associated one-parameter damage laws. Then, we briefly describe the multiaxial fatigue behaviour of the notched round bar under proportional bending-torsion loading. Finally, we compute the multiaxial fatigue lifetime for the different models and compare the predictive capabilities based on a statistical study.

4.1 Uniaxial low-cycle fatigue response

Figure 4 plots the uniaxial low-cycle fatigue response of the tested material at different strain amplitudes evaluated with different dependent parameters, namely stress amplitude, plastic strain amplitude, total strain energy density, and SWT damage parameter. Regardless of the strain amplitude or the dependent parameter, we can distinguish three main stages for each test. At the beginning, i.e. for a dimensionless life about 5-10%, there is a rapid change, followed by a saturated region which occupies most of the test. In a final stage, whose extent is about 5-10% of the dimensionless life, the cyclic response exhibits a sudden change, which culminates with the total failure. This behaviour is in line with that reported in the literature for this steel when subjected to strain-control mode [34].

From the analysis of Figure 4(a) we can identify a cyclic strain-softening response for the entire range of strain amplitude studied in this research [34]. At a fixed strain amplitude, we can see a clear reduction of stress amplitude, with the increase of number of cycles, until a stable stage

is reached. Furthermore, this reduction of stress amplitude during the test corresponds to a reduction of elastic strain amplitude and, consequently, an increase of plastic strain amplitude, which agrees with the trends shown in Figure 4(b). Based on the same reasoning, it is expected that the total strain energy density decreases over time (see Figure 4(c)) because both the area of the hysteresis loops and the area of the elastic components tend to be smaller. Regarding the SWT parameter, under fully-reversed strain-controlled conditions, the reduction of stress amplitude leads to smaller values, as exhibited in Figure 4(d).

In a wider perspective, all the above parameters are quite stable throughout the lifetime and strongly depend on the loading level. This fact may explain why many engineering models use them to link the fatigue damage with the expected durability. Based on these findings, and as usual for engineering steels, the functions relating the loading level to the fatigue lifetime were developed from the mid-life hysteresis loops, which are assumed to be representative of the saturated stage. Figure 5 plots the fitted functions for the different dependent parameters selected in this research. The constants of Eqs. (12)-(15) are compiled in Table 5. In any case, there is an excellent correlation between the fatigue damage parameters and the number of reversals to failure, as demonstrated by the coefficients of correlation (R^2) which are relatively similar in the four cases.

4.2 Multiaxial fatigue behaviour

In this notch geometry, the multiaxial fatigue behaviour is governed by both the bending-torsion ratio (B/T) and the orientation of the bending moment with respect to the notch root (θ). The two main effects on the crack initiation sites and the surface crack paths are summarised in Figure 6. Regarding the crack initiation sites, experimental observations are identified by the white circles. For a fixed value of θ , it can be concluded that the decrease of B/T ratio, which corresponds to a reduction of the normal stress level, moves the crack initiation site to locations closer to the curved edge of the geometric discontinuity (see, for instance, the cases of Figure 6(a) and Figure 6(d)). If we fix the B/T ratio (let us consider, for example, the cases of Figures 6(a)-(c)), it is clear that the higher is the value of θ , the closer is the crack initiation site to the curved edge of the notch [36].

As far as the surface crack paths are concerned, there are substantial differences in the trajectories, which can be explained by the complex stress triaxial state at the notch surface resulting from the normal stress to shear stress ratio, the loading orientation, and the shape of

the geometric discontinuity [5, 10, 36-37]. Figures 6(a) and 6(d) show the surface crack paths for two B/T ratios (respectively, $B/T = 2$ and $B/T = 1$) and the same loading orientation (i.e. $\theta = 0^\circ$). We can observe that the trajectories tend to be straighter, as the ratio of the bending moment to the torsion moment increases. In relation to the effect of the loading orientation, the results indicate that the higher the value of θ , the higher the curvate of the surface crack path (see, for example, Figures 6(d)-(f)).

The crack initiation sites and the crack paths can be successfully predicted via the first principal stress field at the notch surface. The former variable was determined a priori from the surface node with the maximum value of the first principal stress. The predicted locations are identified by the white square symbols in Figure 6. As can be seen, both the experimental observations and the numerical predictions are quite close, irrespective of the loading scenario. Concerning the surface crack paths, the most likely trajectories, represented by the white dashed lines, were computed from the crack initiation site following the nodes with higher values of the first principal stress along the notch surface. A close look at Figure 6 shows that both the experimental observations and the predicted surface crack paths are in good agreement [35,36]. More details about the numerical predictions of crack initiation sites and surface crack paths can be found in the paper by Branco et al. [36].

The fracture surfaces, acquired via optical three-dimensional non-contact focus-variation microscope equipped with a 10× magnification lens, may provide important clues on the complex nature of the fatigue process in this geometry when subjected to bending-torsion loading. The increase of θ , irrespective of the B/T ratio, increases the degree of out-of-plane propagation and makes the crack fronts more curved (see Figures 7(a)-(c) or Figure 7(d)-(e)). In addition, it can be also seen significant differences regarding the crack front shapes marked on fracture surfaces. For $\theta = 0^\circ$, see Figures 7(a) and 7(d), the cracks initiate as surface cracks, and then propagate as through cracks. Nevertheless, for $\theta = 45^\circ$ (see Figure 7(b) and Figure 7(e)), the cracks also initiate as surface cracks but then evolve to corner cracks and only at a final stage become through cracks. Regarding the case of $\theta = 90^\circ$ (see Figure 7(c) and Figure 7(f)), although the initial stage is similar to the others, the crack propagates mostly as a corner crack.

4.3 Fatigue life assessment

The fatigue life assessment, as explained in Section 2, starts with the reduction of the multiaxial stress state to an equivalent uniaxial stress state (see Figure 1(a)), which is done

through the von Mises stress. Then, an averaged stress range ($\Delta\sigma_{eff}$) is computed using the Line Method of the Theory of Critical Distances (see Figure 1(b)). In this study, the stress profile at a line emanating from the crack initiation site in a direction normal to the geometric discontinuity is used for TCD analysis.

The typical von Mises stress profiles found for the different B/T ratios and loading orientations are displayed in Figure 8. For the sake of comparability, the analysis is conducted in a dimensionless form: von Mises stress range ($\Delta\sigma_{eq}$) is divided by the maximum value ($\Delta\sigma_{eq,max}$) and the distance from the initiation site is divided by the critical distance of the Line Method ($D_{LM} = 2a_0$). An interesting outcome is that the stress functions are quite similar, particularly in the region bounded by the critical distance, irrespective of the loading case. This means that the effective stress range (represented by the dot-dashed line for $B/T=2$ (0°)) is approximately equal to 83-85% of the maximum von Mises stress range.

The effective von Mises stress range may be used to compute a uniaxial stress-strain curve representative of the loading scenario. As referred to above, in this research, three different approaches are employed (see Section 2.2). An example of the final hysteresis loop computed for $B/T=1$ (0°) with a nominal normal stress equal to 298.4 MPa (see Table 4) using the ESED rule is presented in Figure 9. Point A ($\sigma_{max}, \epsilon_{max}$) was calculated through Eq. (5) along with the Ramberg-Osgood relationship. Point B ($\Delta\sigma, \Delta\epsilon$) was determined with respect to a coordinate system centred at Point A using Eq. (6) and the Masing model. From the generated hysteresis loop, the required values of the fatigue damage parameters were calculated. Then, the procedure was repeated for the various loading cases and the three local stress-strain approaches.

Fatigue life can be assessed by inserting the values of the fatigue damage parameters previously calculated into the uniaxial functions obtained in the low-cycle fatigue tests (see Section 4.1). Figure 10 plots the experimental lives (N_i) against the predicted results (N_p) determined via the Neuber's rule. For the sake of clarity, scatter bounds with factors of two (i.e. $N_i = 2N_p$ and $N_p = 2N_i$) were drawn. It is clear that energy-based predictions are more accurate than the others. In this method, all points are correlated, either for shorter lives or longer lives. On the contrary, stress-based predictions are too conservative, particularly at higher strain levels. Both the strain-based and the SWT-based models led to intermediate results, reasonably correlated in the entire range, but tendentially conservative.

Regarding the ESED rule, the experimental lives (N_i) and the predicted results (N_p) for the different fatigue models are displayed in Figure 11. Overall, the general trends are relatively similar to those described in the previous case. Nevertheless, although the stress-based model also shows a great scatter, both the strain-based and the SWT-based predictions are more balanced, exhibiting more points within the bounds. As far as the energy-based model is concerned, predictions maintain an excellent correlation with the experimental lives. The better results associated with the ESED rule can be explained by the fact that Neuber's rule tends to overestimate the strain field at the notch root, which is likely to lead to shorter lives.

The fatigue life predictions determined with the modified ESED rule for the four one-parameter damage laws selected in this paper are shown in Figure 12. In this case, there are no obvious differences regarding the original ESED rule. Similarly, the stress-based model leads to an identical scatter, with most points out of the bounds, particularly in the low-cycle fatigue regime. Strain-based and SWT-based predictions also maintain the same trends, with most points at the conservative side. Finally, the energy-based results continue to be the most accurate, strongly agreeing with the experimental observations.

In order to better evaluate the predictive capabilities of the tested methods, a comparative analysis of the fatigue error, computed in the form of a probability density function was carried out. The fatigue error (E_N) was defined by the following equation:

$$E_N = \log_{10} \left(\frac{N_i}{N_p} \right) \quad \text{Eq. (16)}$$

and the probability density function ($Z(x)$) was defined by the formula:

$$Z(x) = \frac{1}{\rho \sqrt{2\pi}} e^{-\frac{(x-\mu)^2}{2\rho^2}} \quad \text{Eq. (17)}$$

where ρ is the standard deviation and μ is the mean value.

Figure 13 shows the probability density functions of the fatigue errors for the three local stress-strain approaches and the four one-parameter damage laws tested here. More accurate models are generally associated with lower standard deviations and mean errors closer to zero. The errors associated with the energy-based calculations, irrespective of the local stress-

strain approach, are much closer to zero than the others, which is confirmed by the smaller mean values and the lower standard deviations. The other three models are tendentially displaced towards the safe area. Both the strain-based and the stress-based results are quite similar. Nevertheless, the former leads to smaller mean values and lower standard deviations. Concerning the stress-based model, the predictive capabilities are clearly less reliable than the others.

It can also be noted an important improvement of fatigue life predictions when the ESED and the modified ESED rules are applied, independently of the fatigue damage parameter considered in the calculations. Furthermore, although the differences are not significant, the modified ESED rule led to smaller standard deviations, in all cases, than the original ESED rule. In a macro perspective, we can also conclude that the energy-based formulation is reliable to estimate the fatigue lifetime in U-shaped notches subjected to proportional bending-torsion loading when combined with any of the three local stress-strain approaches studied here. Both the strain-based and the SWT-based methods are also capable of predicting the fatigue life expectancy for this geometry and the tested loading scenarios. It is worth to note that the three approaches require similar computational cost, which is another interesting outcome.

The present approach can be easily extended to more complex geometries that can be obtained by additive processes [38-40] and more complex loading conditions [41-42]. Future developments will include the possibility to fully compute three-dimensional effects [43-44], which sometimes play a fundamental role in the final fatigue life.

5. Conclusions

This paper aimed at comparing the predictive capabilities of different fatigue models developed by combining various uniaxial damage parameters and various local stress-strain approaches in notched components subjected to bending-torsion loading. Four well-known models (stress-based, strain-based, SWT-based, and energy-based) were selected to correlate the loading level and the fatigue durability using uniaxial low-cycle fatigue results. Cyclic plasticity at the notch-controlled process zone was accounted for numerically, within a linear-elastic framework, by reducing the multiaxial stress state to an equivalent uniaxial stress state (von Mises stress range) using a local stress-strain approach (Neuber's rule, ESED rule, or modified ESED rule) and the Theory of Critical Distances. The following conclusions can be drawn:

- (1) regardless of the strain amplitude, the cyclic response of the tested steel was quite stable throughout the entire lifetime, enabling the definition of stress-based, strain-based, SWT-based, and energy-based functions with high correlation coefficients between the above parameters and the fatigue lifetime;
- (2) irrespective of the local stress-strain approach, the stress-based method tended to be too conservative, particularly for lower lives; on the contrary, the other three methods led to good correlations between the experimental observations and the predicted lifetime;
- (3) the energy-based model showed the best predictive capabilities, regardless of the rule introduced to account for the cyclic plasticity effect at the notch-controlled region. Errors were relatively balanced, sometimes conservative, other times non-conservative, but much closer to zero and with lower standard deviations;
- (4) Neuber's rule led to more conservative results which was associated with the overestimation of strain fields at the notch root. Concerning the rules based on the strain energy density, although the differences were not significant, the modified ESED rule was slightly more accurate than the original ESED rule.

Acknowledgements

This research is sponsored by FEDER funds through the program COMPETE – Programa Operacional Factores de Competitividade – and by national funds through FCT – Fundação para a Ciência e a Tecnologia –, under the project UIDB/00285/2020.

References

1. Socie D, Marquis G. Multiaxial fatigue. SAE International; 1999. ISBN 978-0768004533.
2. Carpinteri A, Spagnoli A, Vantadori S, Viappiani D. A multiaxial criterion for notch high-cycle fatigue using a critical-point method. *Eng. Fract. Mech.* 2008;75:1864–74.
<https://doi.org/10.1016/j.engfracmech.2006.11.002>.
3. Zhu SP, He JC, Liao D, Wang Q, Liu Y. The effect of notch size on critical distance and fatigue life predictions. *Mater. Des.* 2020;196:109095.
<https://doi.org/10.1016/j.matdes.2020.109095>
4. Papadopoulos I, Davoli P, Gorla C, Filippini M, Bernasconi A. A comparative study of multiaxial high-cycle fatigue criteria for metals. *Int. J. Fatigue* 1995;19:219–35.
[https://doi.org/10.1016/S0142-1123\(96\)00064-3](https://doi.org/10.1016/S0142-1123(96)00064-3).

5. Karolczuk A, Macha E. A review of critical plane orientations in multiaxial fatigue failure criteria of metallic materials. *Int. J. Frac.* 2005;134:267–304.
<https://doi.org/10.1007/s10704-005-1088-2>.
6. Carpinteri A, Spagnoli A, Vantadori S (2011). Multiaxial fatigue assessment using a simplified critical plane-based criterion. *Int. J. Fatigue* 2011;33, 969–976.
<https://doi.org/10.1016/j.ijfatigue.2011.01.004>
7. Goncalves CA, Araùjo JA, Mamiya EN. Multiaxial fatigue: a stress based criterion for hard metals. *Int. J. Fatigue* 2005;27:177–87. <https://doi.org/10.1016/j.crme.2004.09.003>
8. Branco R, Prates PA, Costa JD, Berto F, Kotousov A. New methodology of fatigue life evaluation for multiaxially loaded notched components based on two uniaxial strain-controlled tests. *Int. J. Fatigue* 2018;111:308-320.
<https://doi.org/10.1016/j.ijfatigue.2018.02.027>
9. Li DH, Shang DG, Xue L, Li LJ, Wang LW, Cui J. Notch stress-strain estimation method based on pseudo stress correction under multiaxial thermo-mechanical cyclic loading. *Int. J. Solids Struct.* 2020;199:144-157. <https://doi.org/10.1016/j.ijsolstr.2020.04.002>
10. Branco R, Costa JD, Martins Ferreira J, Capela C, Antunes FV, Macek W. Multiaxial fatigue behaviour of maraging steel produced by selective laser melting. *Mater. Des.* 2021;109469.
<https://doi.org/10.1016/j.matdes.2021.109469>
11. Susmel L, Taylor D. A novel formulation of the theory of critical distances to estimate lifetime of notched components in the medium-cycle fatigue regime. *Fatigue Fract. Eng. Mater. Struct.* 2007;30:567–81. <https://doi.org/10.1111/j.1460-2695.2007.01122.x>
12. Liao D, Zhu SP, Correia JAFO, De Jesus AMP, Berto F. Recent advances on notch effects in metal fatigue: A review. *Fatigue Fract. Eng. Mater. Struct.* 2020;43:637-659.
<https://doi.org/10.1111/ffe.13195>
13. Taylor D. Geometrical effects in fatigue: a unifying theoretical model. *Int. J. Fatigue* 1999;21:413–20. [https://doi.org/10.1016/S0142-1123\(99\)00007-9](https://doi.org/10.1016/S0142-1123(99)00007-9).
14. Lazzarin P, Zambardi R. A finite-volume-energy based approach to predict the static and fatigue behaviour of components with sharp V-shaped notches. *Int. J. Fract.* 2001;112:275–298. <https://doi.org/10.1023/A:1013595930617>
15. Berto F, Lazzarin P. Recent developments in brittle and quasi-brittle failure assessment of engineering materials by means of local approaches. *Mater. Sci. Eng. R Reports* 2014;75:1–48. <https://doi.org/10.1016/j.mser.2013.11.001>.
16. Ayatollahi MR, Rashidi Moghaddam M, Berto F. A generalized strain energy density criterion for mixed mode fracture analysis in brittle and quasi-brittle materials.



- Theor. Appl. Fract. Mech. 2015;79:70–6.
<https://doi.org/10.1016/j.tafmec.2015.09.004>.
17. Berto F, Barati E. Fracture assessment of U-notches under three point bending by means of local energy density. *Mater. Des.* 2011;32:822–30.
<https://doi.org/10.1016/j.matdes.2010.07.017>.
 18. Ellyin F, Kujawski D. Notch root stress/strain prediction for elastic-plastic loading. *Res. Mech.* 1987;20:177–190.
 19. G. Lesiuk, M. Szata, D. Rozumek, Z. Marciniak, J. Correia, De Jesus, A. Energy response of S355 and 41Cr4 steel during fatigue crack growth process. *J. Strain Anal. Eng. Des.* 2018;53:663-675. <https://doi.org/10.1177/0309324718798234>
 20. Hu Z, Berto F, Hong Y, Susmel L. Comparison of TCD and SED methods in fatigue lifetime assessment. *Int. J. Fatigue* 2019;123:105-134.
<https://doi.org/10.1016/j.ijfatigue.2019.02.009>
 21. Lutovinov M, Cerny J, Papuga J. A comparison of methods for calculating notch tip strains and stresses under multiaxial loading. *Frat. ed Integrita Strutt.* 2016;38:237-243.
 22. Zappalorto M, Kujawski D. Neuber's rules and other solutions: Theoretical differences, formal analogies and energy interpretations. *Theor. Appl. Fract. Mech.* 2015;79:2–13.
<https://dx.doi.org/10.1016/j.tafmec.2015.07.010>
 23. Taylor D. The Theory of Critical Distances: a link to micromechanisms. *Theor. Appl. Fract. Mech.* 2017; 90:228-233. <https://doi.org/10.1016/j.tafmec.2017.05.018>
 24. Neuber H. Theory of stress concentration for shear strained prismatical bodies with arbitrary non-linear stress-strain law. *J. Appl. Mech.* 1961;28:544–550.
 25. Molski K, Glinka G. A method of elastic–plastic stress and strain calculation at a notch root. *Mater. Sci. Eng.* 50 1981;50:93–100. [https://doi.org/10.1016/0025-5416\(81\)90089-6](https://doi.org/10.1016/0025-5416(81)90089-6)
 26. Ye DY, Matsuoka S, Suzuki N, Maeda Y. Further investigation of Neuber's rule and the equivalent strain energy density (ESED) method. *Int. J. Fatigue* 2004;26:447-455.
<https://doi.org/10.1016/j.ijfatigue.2003.10.002>
 27. Ellyin F. *Fatigue Damage, Crack Growth and Life Prediction*, Chapman & Hall, London, 1997.
 28. Morrow JD (1965). *Cyclic plastic strain energy and fatigue of metals*. International Friction, Damping and Cyclic Plasticity, American Society for Testing and Materials, ASTM STP 378, Philadelphia, 45-87.
 29. Manson SS (1954). *Behaviour of materials under conditions of thermal stress*. NACA TN-2933, National Advisory Committee for Aeronautics.

30. Coffin LF (1954). A study effects of cyclic thermal stresses on ductile metal. Transactions of ASME 76, 931-950.
31. Golos K, Ellyin F. Generalization of cumulative damage criterion to multilevel cyclic loading. Theor. Appl. Fract. Mech. 1987;7:169–176. [https://doi.org/10.1016/0167-8442\(87\)90032-2](https://doi.org/10.1016/0167-8442(87)90032-2)
32. Smith KN, Watson P, Topper TH. A stress-strain function for the fatigue of metals. J. Mater. 197;5:767–778.
33. Correia J, Apetre N, Arcari A, Jesus A, Muñiz-Calvente M, Calçada R, Berto F, Fernández-Canteli A. Generalized probabilistic model allowing for various fatigue damage variables. Int. J. Fatigue 2017;100:187-194. <https://doi.org/10.1016/j.ijfatigue.2017.03.031>
34. Branco R, Costa JD, Antunes FV. Low-cycle fatigue behaviour of 34CrNiMo6 high strength steel. Theor. Appl. Fract. Mech. 2012;58:28–34. <https://doi.org/10.1016/j.tafmec.2012.02.004>
35. Branco R, Costa JD, Antunes FV. Fatigue behaviour and life prediction of lateral notched round bars under bending–torsion loading. Eng. Fract. Mech. 2014;119:66–84. <https://doi.org/10.1016/j.engfracmech.2014.02.009>
36. Branco R, Costa JD, Berto F, Antunes FV. Effect of loading orientation on fatigue behaviour in severely notched round bars under non-zero mean stress bending-torsion. Theor. Appl. Fract. Mech. 2017;92:185–97. <https://doi.org/10.1016/j.tafmec.2017.07.015>.
37. Rozumek D, Marciniak Z, Lesiuk G, Correia JAFO. Mixed mode I/II/III fatigue crack growth in S355 steel. Procedia Structural Integrity 2017;5:896-903. <https://doi.org/10.1016/j.prostr.2017.07.125>
38. Razavi SMJ, Ferro P, Berto F, Torgersen J. Fatigue strength of blunt V-notched specimens produced by selective laser melting of Ti-6Al-4V. Theor. Appl. Fract. Mech. 2018;97:376–384. <https://doi.org/10.1016/j.tafmec.2017.06.021>.
39. Wu W, Hu W, Qian G, Liao H, Xu X, Berto F (2019). Mechanical design and multifunctional applications of chiral mechanical metamaterials: A review. Mater. Des. 180, 107950. <https://doi.org/10.1016/j.matdes.2019.107950>
40. Benedetti M, du Plessis A., Ritchie R.O., Dallago M., Razavi S.M.J., Berto F. Architected cellular materials: A review on their mechanical properties towards fatigue-tolerant design and fabrication. Mater. Sci. Eng. R: Reports 2021;144, 100606. <https://doi.org/10.1016/j.mser.2021.100606>.
41. Cruces AS, Mokhtarishirazabad M, Moreno B, Zanganeh M, Lopez-Crespo P. Study of the biaxial fatigue behaviour and overloads on S355 low carbon steel. Int. J. Fatigue 2020;134: 105466. <https://doi.org/10.1016/j.ijfatigue.2019.105466>

42. Marciniak Z, Rozumek D, Macha E. Fatigue lives of 18G2A and 10HNAP steels under variable amplitude and random non-proportional bending with torsion loading. *Int. J. Fatigue* 2008;30:800-813.
43. Berto F, Lazzarin P, Wang CH. Three-dimensional linear elastic distributions of stress and strain energy density ahead of V-shaped notches in plates of arbitrary thickness. *Int. J. Fract.* 2004;127:265–82. <https://doi.org/10.1023/B:FRAC.0000036846.23180.4d>.
44. Berto F, Lazzarin P, Kotousov A. On higher order terms and out-of-plane singular mode. *Mech. Mater.* 2011;43:332–41. <https://doi.org/10.1016/j.mechmat.2011.03.004>.

Nomenclature

$2N_f$	number of reversals to failure
a_0	material characteristic length
b	fatigue strength exponent
B/T	bending moment to torsion moment ratio
c	fatigue strength exponent
D_{LM}	critical distance of the Line Method
E	Young's modulus
E_N	fatigue error
k	strain hardening coefficient
k'	cyclic strain hardening coefficient
k_t	stress concentration factor
n	strain hardening exponent
n'	cyclic strain hardening exponent
N_i	number of cycles to fatigue crack initiation
N_f	number of cycles to failure

N_p	predicted fatigue life
r	distance from the crack initiation site
R^2	coefficient of determination
S	nominal stress
$Z(x)$	probability density function
α_t	material constant
α	material constant
ΔK_{th}	threshold value of the stress intensity factor range
ΔW_{0t}	tensile elastic energy at the material fatigue limit
ΔW_{e+}	elastic positive strain energy density
ΔW_p	plastic strain energy density
ΔW_t	total strain energy density
ΔS	nominal stress range
$\Delta \varepsilon$	local strain range
$\Delta \sigma$	local stress range
$\Delta \sigma_0$	material plain fatigue limit
$\Delta \sigma_{eff}$	effective stress range
$\Delta \sigma_{eq}$	equivalent von Mises stress range
$\Delta \sigma_{eq,max}$	maximum value of the equivalent von Mises stress range
ε	local strain
ε_a	strain amplitude
ε'_f	fatigue ductility coefficient
ε_m	mean strain
ε_{max}	maximum strain
θ	bending moment angle
κ	material constant
κ_t	material constant
ρ	standard deviation
μ	mean value
σ	local stress
σ_a	stress amplitude

σ'_f	fatigue strength coefficient
σ_m	mean stress
σ_{max}	maximum stress
ν	Poisson's ratio
ψ	fatigue damage parameter
ψ_0	fatigue limit

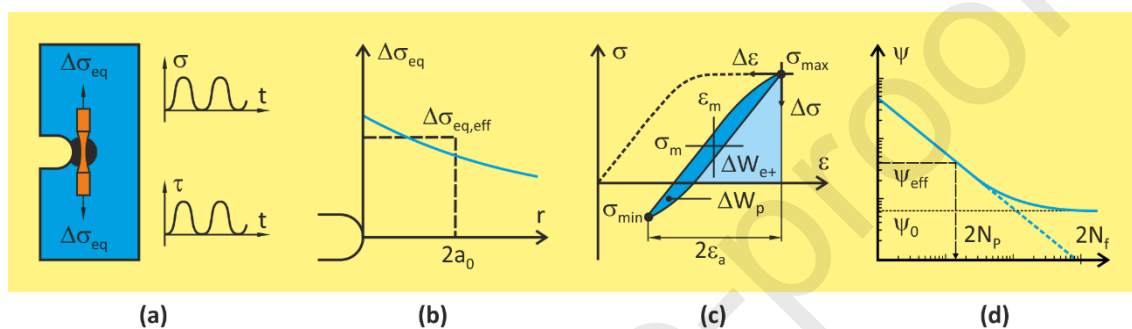


Figure 1. Overview of fatigue life assessment approaches: (a) reduction of multiaxial stress state to an equivalent uniaxial stress state; (b) calculation of an effective stress range; (c) generation of a cyclic stress-strain hysteresis loop; and (d) estimation of fatigue lifetime.

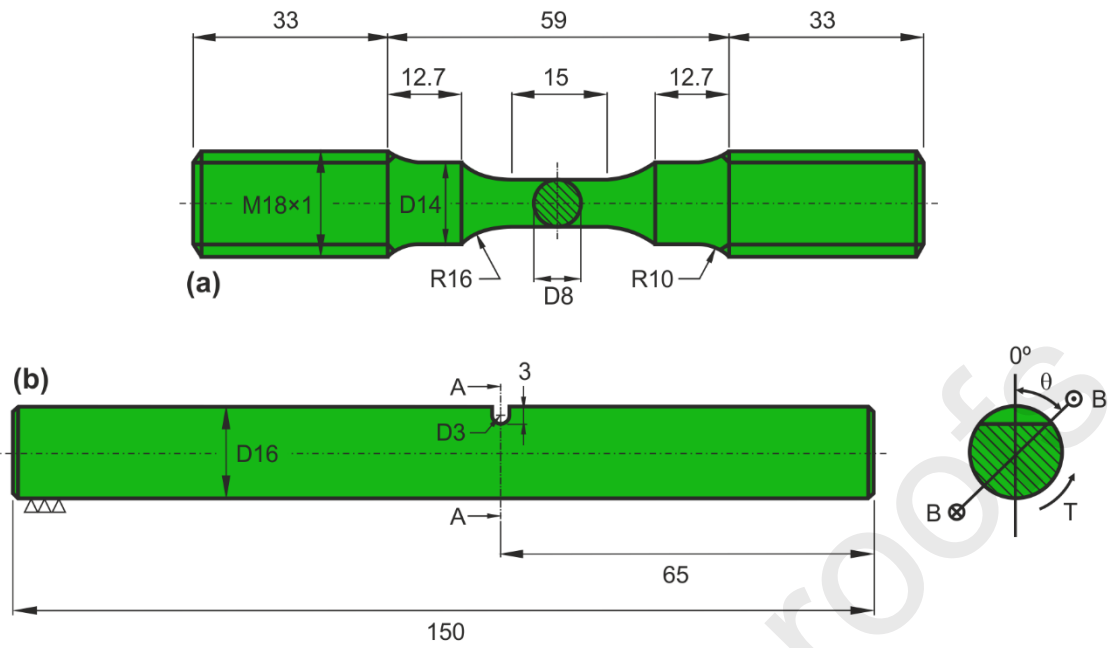


Figure 2. Specimen geometries of the: (a) uniaxial low-cycle fatigue tests; and (b) multiaxial bending-torsion fatigue tests (unit: mm).

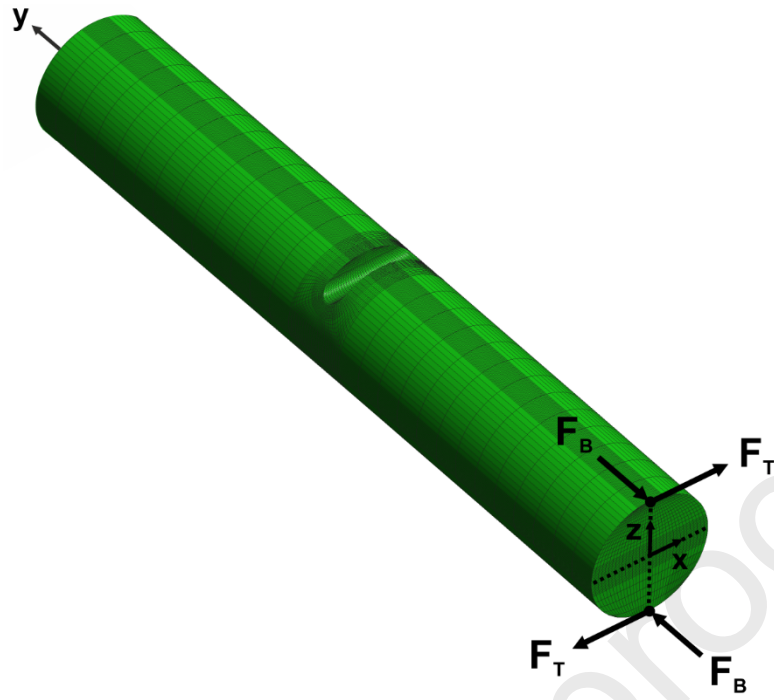


Figure 3. Finite element model developed to assess the stress-strain fields at the notch root for the bending-torsion tests. F_B represents the pair of forces applied to generate the bending moment and F_T represents the pair of forces to generate the torsion moment.

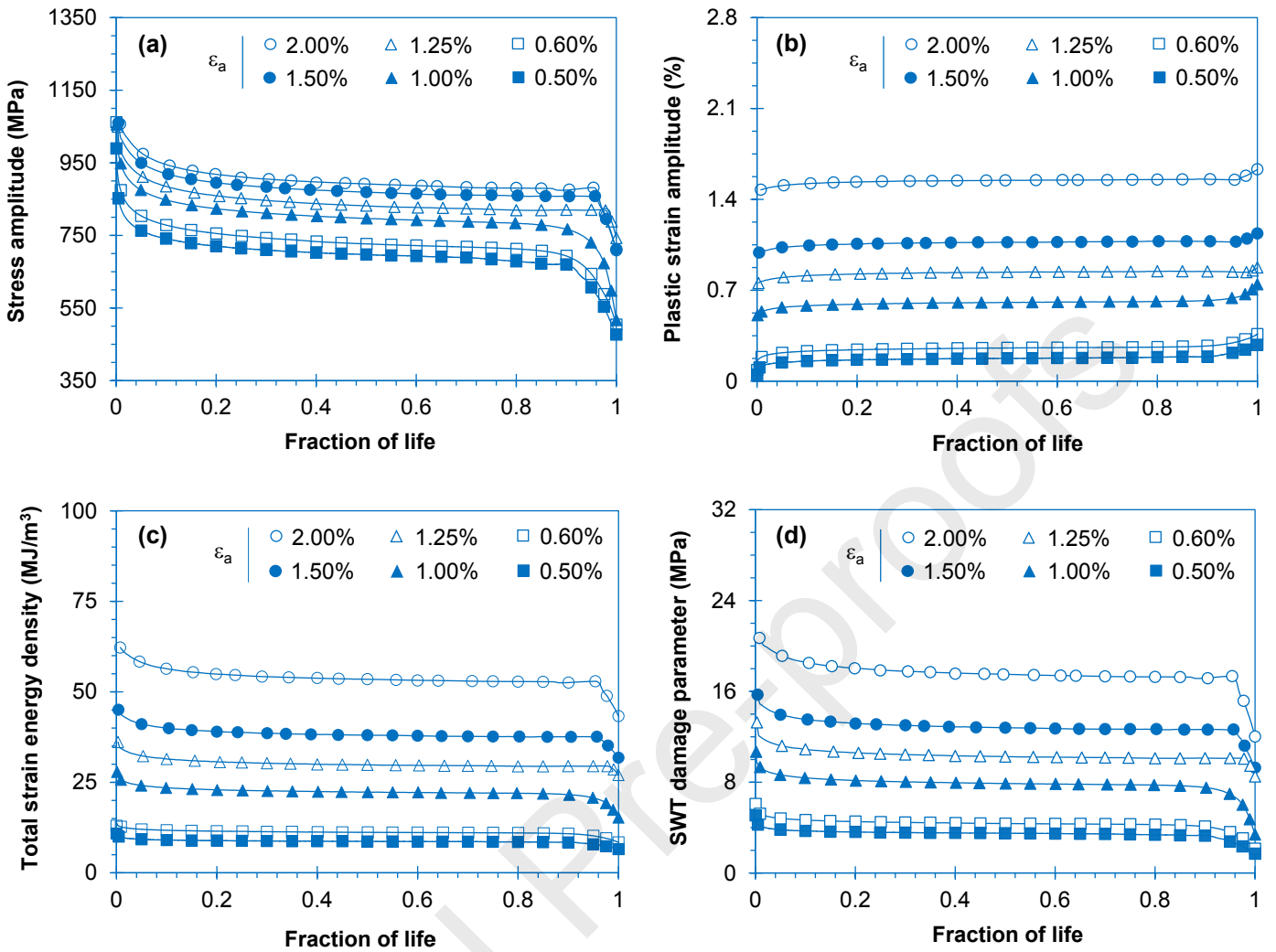


Figure 4. Uniaxial low-cycle fatigue response under strain-controlled conditions at different strain amplitudes: (a) stress amplitude against dimensionless life; (b) plastic strain amplitude against dimensionless life; (c) total strain energy density against dimensionless life; and (d) SWT parameter against dimensionless life.

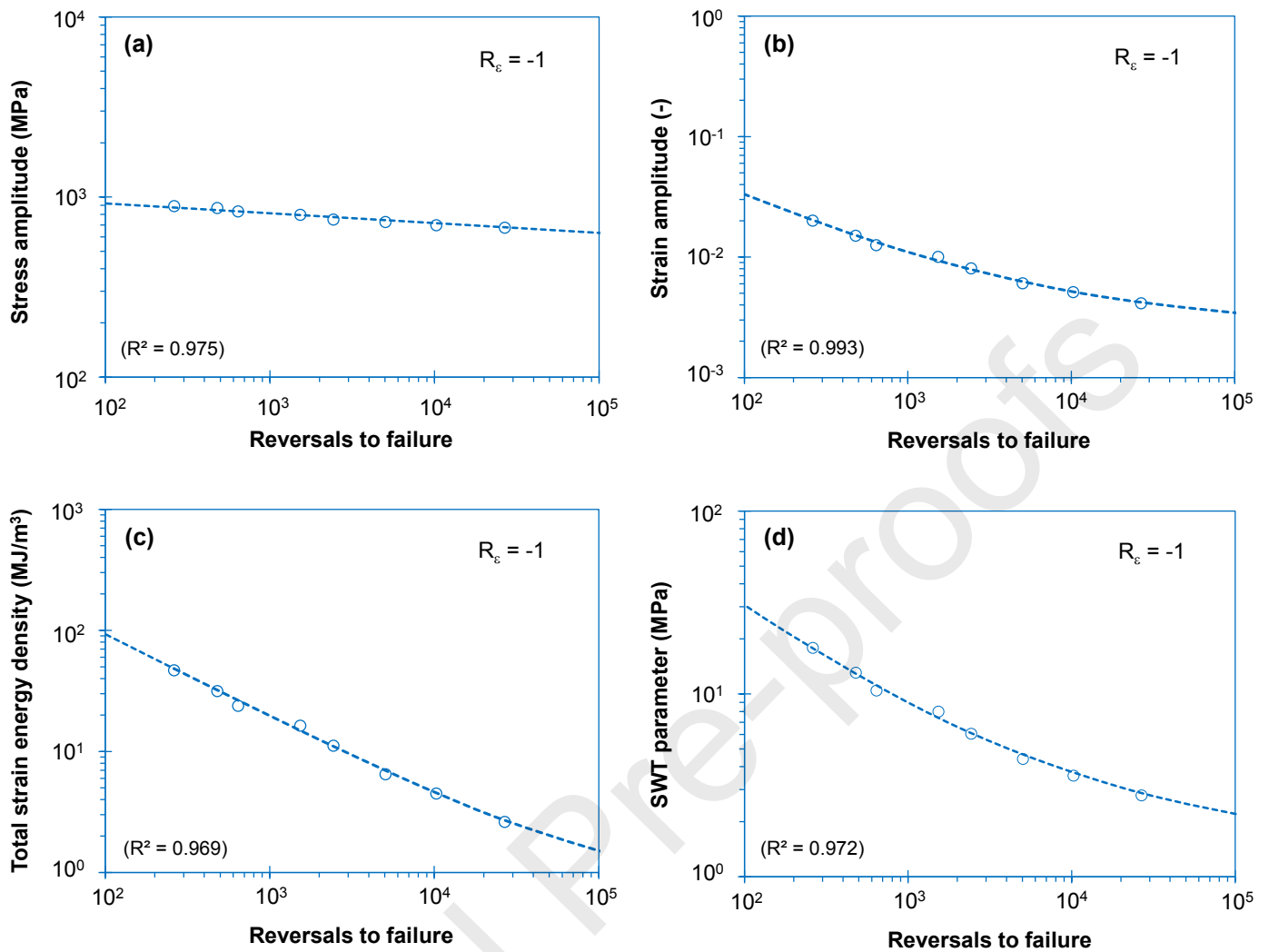


Figure 5. One-parameter damage laws computed from low-cycle fatigue tests using the half-life cycles: (a) stress amplitude versus number of reversals to failure; (b) strain amplitude versus number of reversals to failure; (c) total strain energy density versus number of reversals to failure; and (d) SWT parameter versus number of reversals to failure.

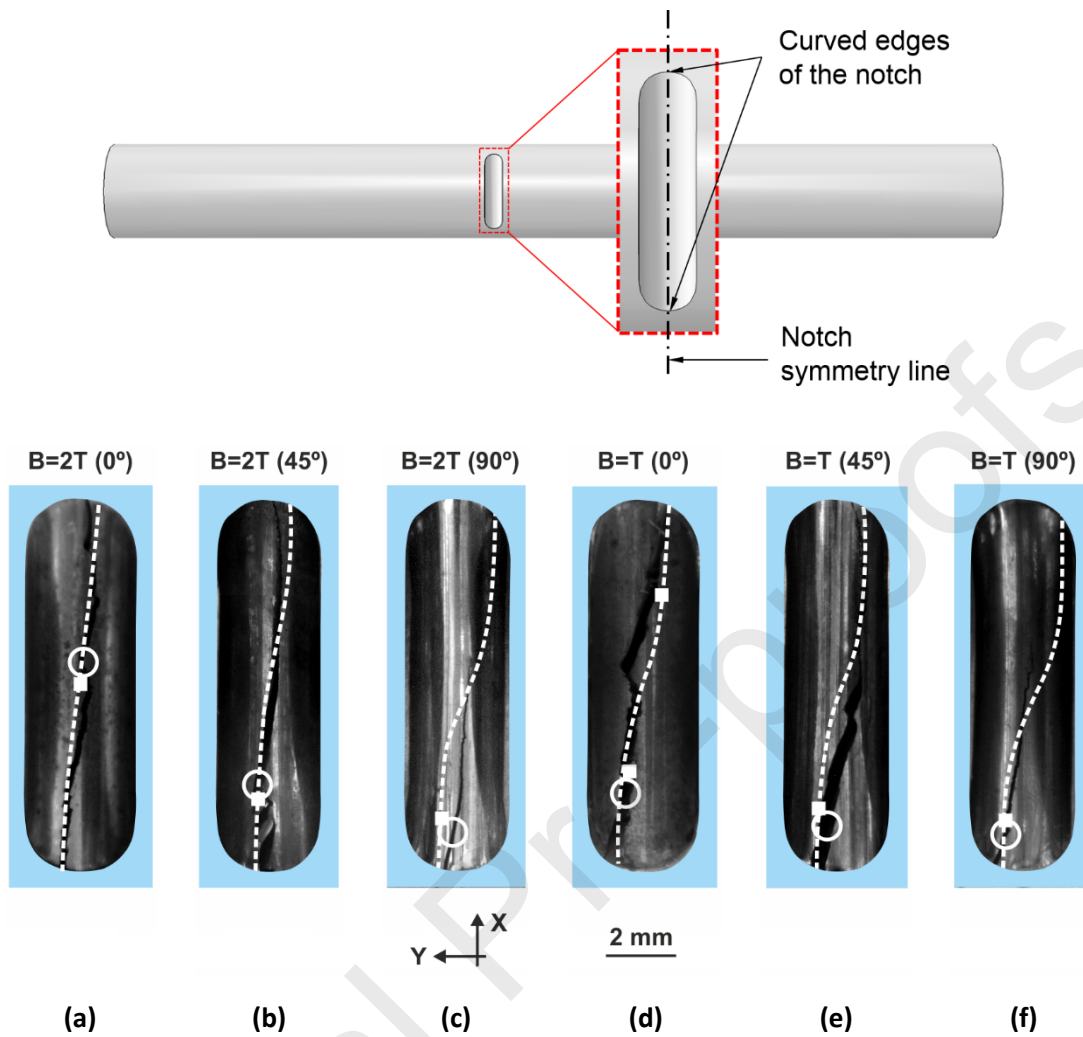


Figure 6. Surface crack paths and crack initiation sites observed in the experiments and predicted numerically: (a) $B/T=2$ (0°); (b) $B/T=2$ (45°); (c) $B/T=2$ (90°); (d) $B/T=1$ (0°); (e) $B/T=1$ (45°); and (f) $B/T=1$ (90°). The white circles represent the experimental crack initiation sites; the white squares represent the predicted initiation sites; and the dashed lines represent the predicted crack paths.

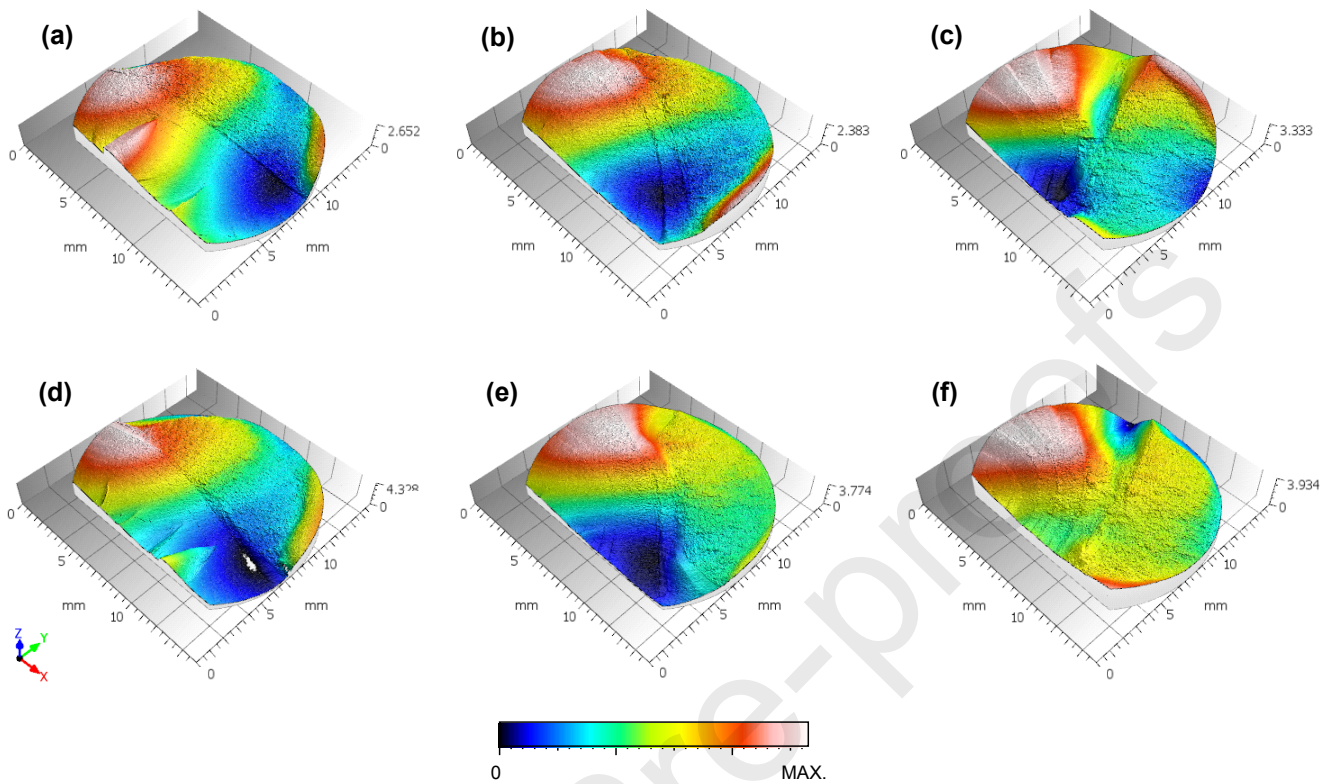


Figure 7. Fracture surfaces acquired via optical focus-variation microscopy: (a) $B/T=2$ (0°); (b) $B/T=2$ (45°); (c) $B/T=2$ (90°); (d) $B/T=1$ (0°); (e) $B/T=1$ (45°); and (f) $B/T=1$ (90°). Pseudo-colour views represent the height from the lowest point of fracture surface measured in the z-axis direction.

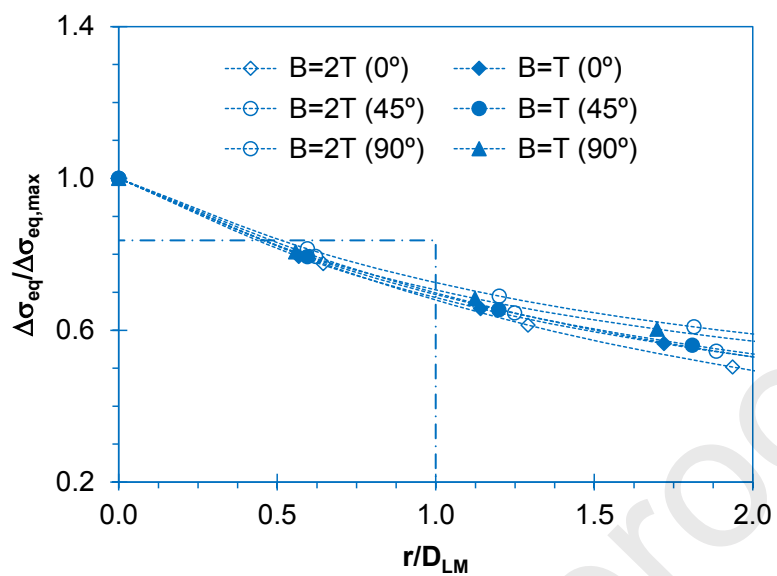


Figure 8. Dimensionless von Mises stress range against the dimensionless distance from the initiation site for the different loading scenarios.

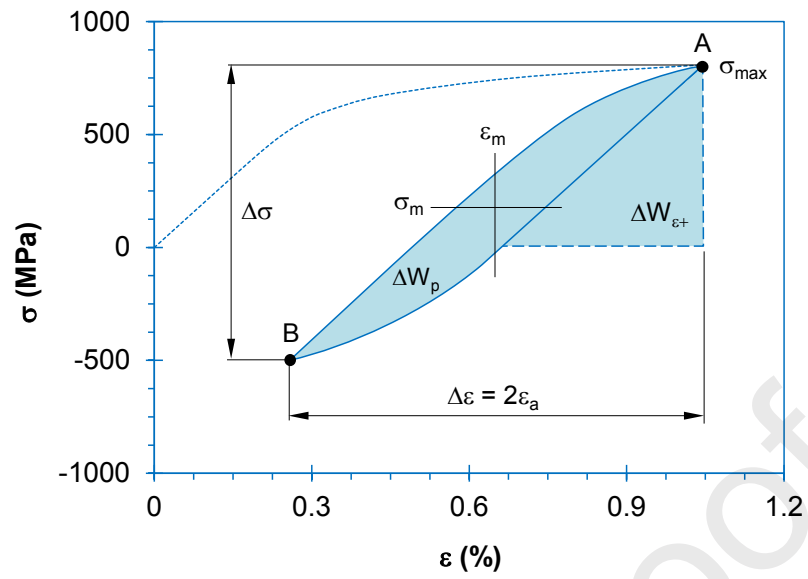


Figure 9. Stress-strain hysteresis loop computed using the ESED rule for $B/T = 1$ (0°) with $\sigma_m = 298.4$ MPa.

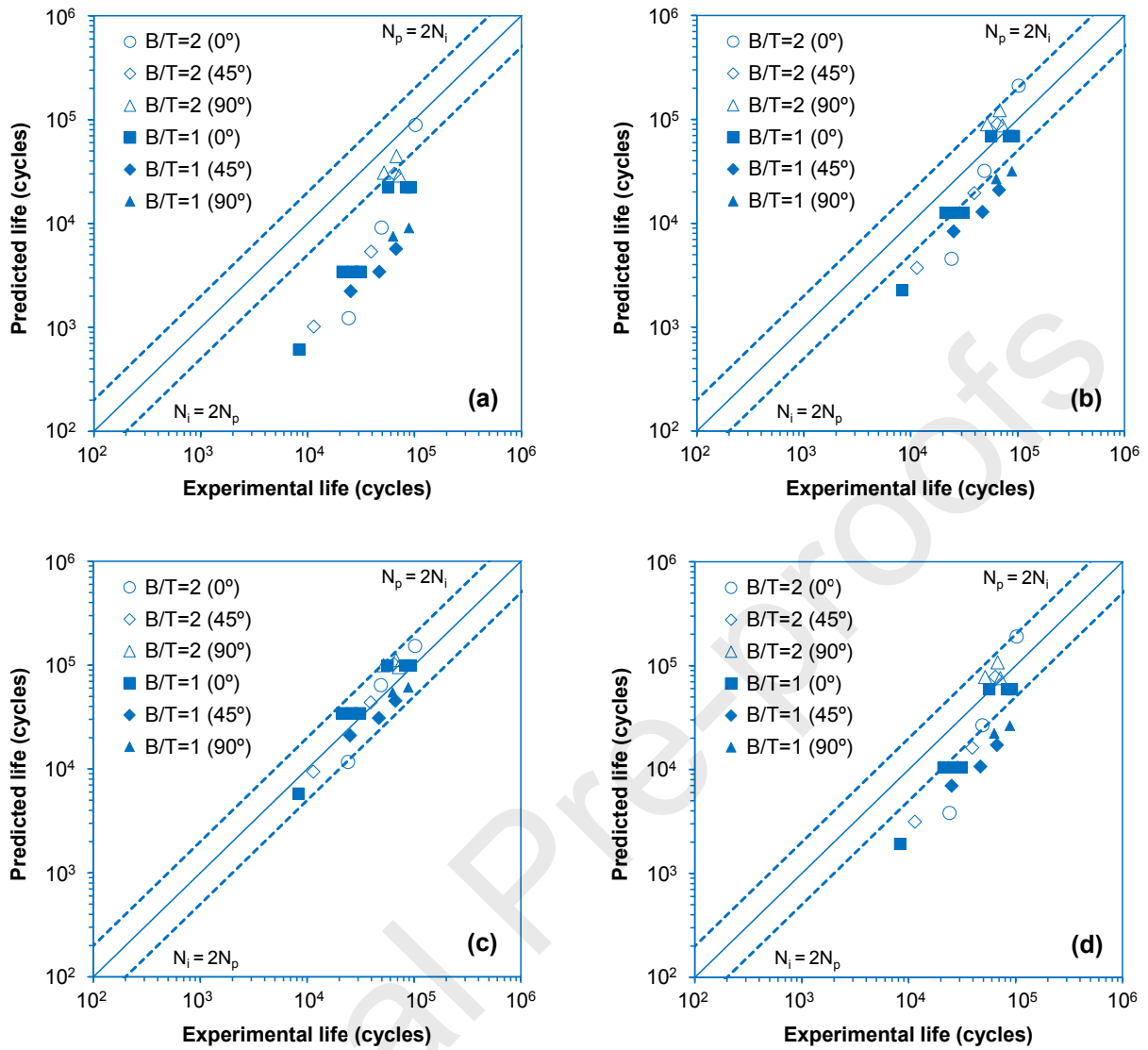


Figure 10. Fatigue life predictions obtained by combining the Neuber's rule and the: (a) stress-based; (b) strain-based; (c) energy-based; and (d) SWT-based models.

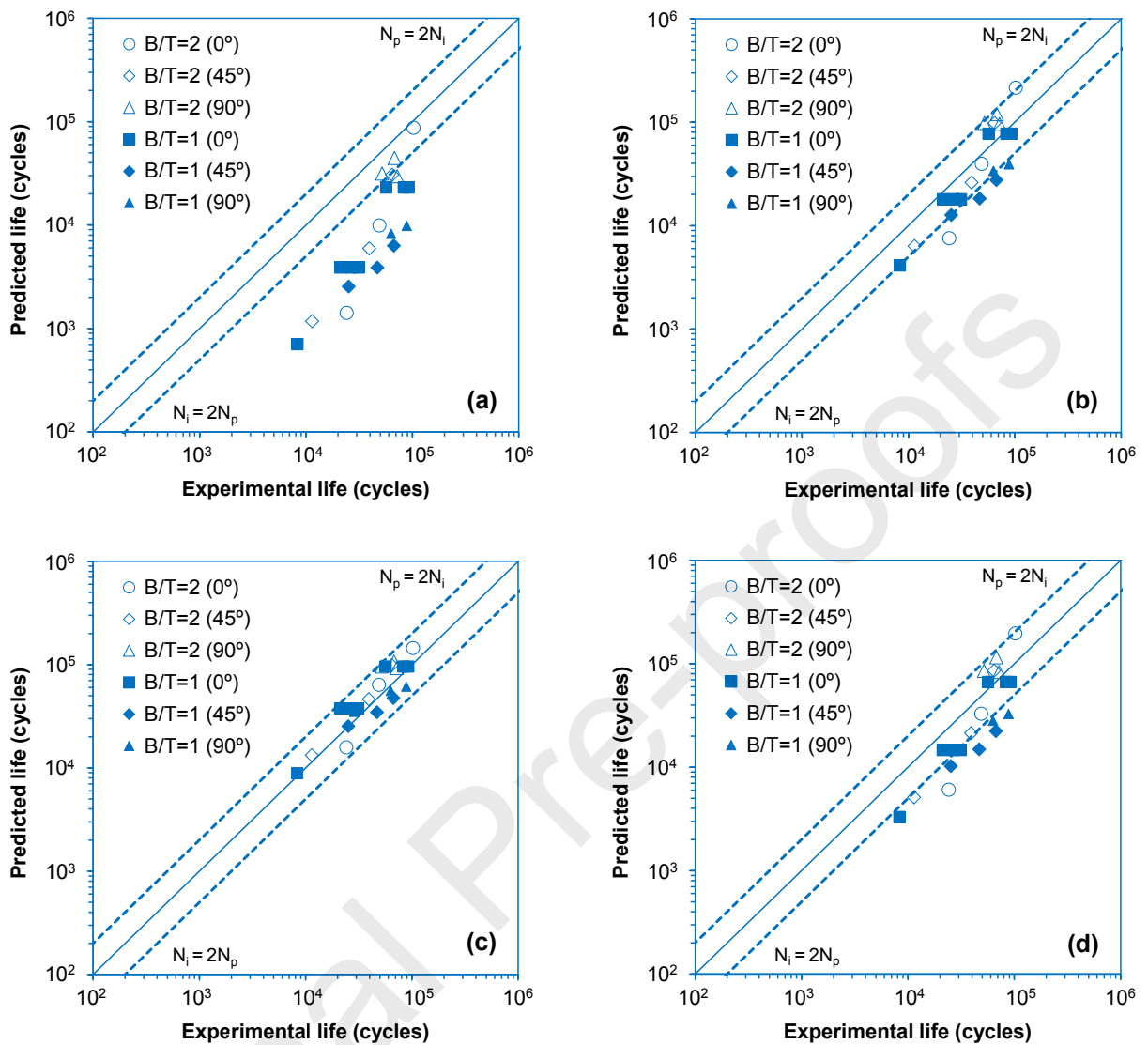


Figure 11. Fatigue life predictions obtained by combining the ESED rule and the: (a) stress-based; (b) strain-based; (c) energy-based; and (d) SWT-based models.

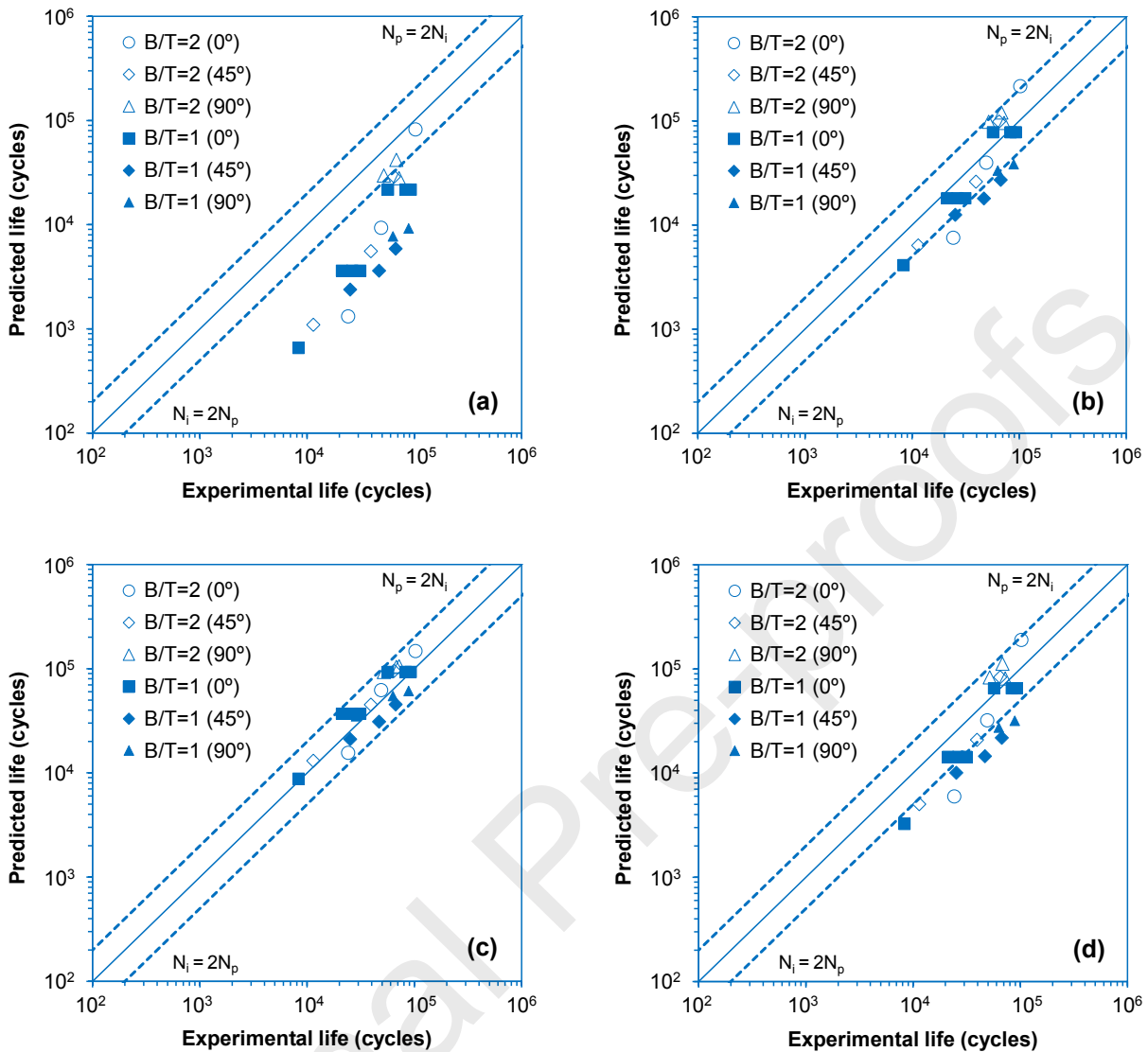


Figure 12. Fatigue life predictions obtained by combining the modified ESED rule and the: (a) stress-based; (b) strain-based; (c) energy-based; and (d) SWT-based models.

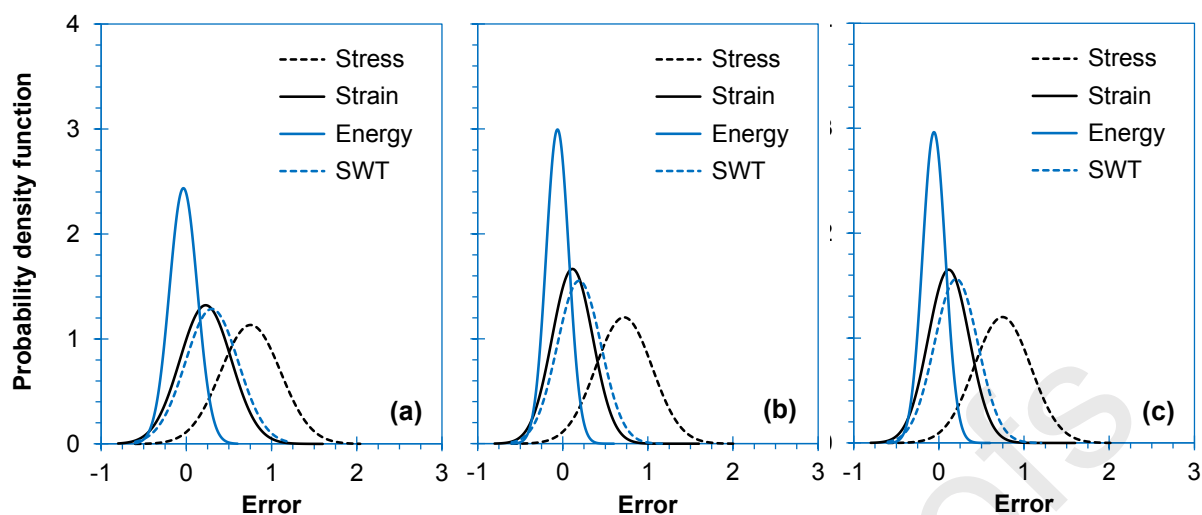


Figure 13. Comparative analysis of the predictive capabilities of the different one-parameter damage laws combined with the: (a) Neuber's rule; (b) ESED rule; and (c) modified ESED rule.

Table 1. Nominal chemical composition of the DIN 34CrNiMo6 (wt%).

C	Si	Mn	Cr	Mo	Ni
0.34	≤ 0.40	0.65	1.50	0.22	1.50

Table 2. Mechanical properties of the 34CrNiMo6 high-strength steel [35].

Mechanical property	Value
Yield strength, σ_{YS} (MPa)	967
Tensile strength, σ_{UTS} (MPa)	1035
Young's modulus, E (GPa)	209.8
Poisson's ratio, ν	0.296
Cyclic strain hardening coefficient, k' (MPa)	1361.6
Cyclic strain hardening exponent, n'	0.1041
Fatigue limit stress range, $\Delta\sigma_0$ (MPa)	353
Stress intensity factor range threshold, ΔK_{th0} (MPa·m ^{0.5})	7.12



Table 3. Summary of low-cycle fatigue tests (half-life cycle).

Test reference	σ_a (MPa)	ε_a (MPa)	ΔW_t (MJ/m ³)	$2N_f$ (reversals)
2.00%	891.8	2.003	45.04	262
1.50%	869.0	1.503	29.83	480
1.25%	831.6	1.254	22.23	642
1.00%	796.8	1.004	14.89	1534
0.80%	750.6	0.806	9.83	2438
0.60%	726.6	0.607	5.26	5046
0.50%	697.5	0.512	3.37	10,280
0.40%	675.3	0.413	1.59	26,756

Table 4. Summary of multiaxial fatigue tests.

Test reference	B/T	θ	σ_a (MPa)	σ_m (MPa)	τ_a (MPa)	τ_m (MPa)	N_i (cycle)
2(0)-1	2	0°	179.1	194.0	44.9	48.5	102,386
2(0)-2	2	0°	223.8	238.7	56.0	59.7	49,103
2(0)-3	2	0°	298.4	313.3	74.6	78.3	24,207
2(45)-1	2	45°	208.9	223.8	52.2	56.0	64,754
2(45)-2	2	45°	253.7	268.6	63.4	67.2	39,331
2(45)-3	2	45°	328.3	343.2	82.1	85.8	11,422
2(90)-1	2	90°	343.0	365.3	85.8	91.3	68,010
2(90)-2	2	90°	356.4	383.1	89.1	95.8	72,072
2(90)-3	2	90°	364.1	379.0	91.0	94.8	51,878
1(0)-1	1	0°	179.1	194.0	89.6	97.0	92,544
1(0)-2	1	0°	179.1	194.0	89.6	97.0	83,278
1(0)-3	1	0°	179.1	194.0	89.6	97.0	56,749
1(0)-4	1	0°	223.8	238.7	112.0	119.4	26,420
1(0)-5	1	0°	223.8	238.7	112.0	119.4	21,225
1(0)-6	1	0°	223.8	238.7	112.0	119.4	31,306
1(0)-7	1	0°	298.4	313.3	149.2	156.7	8314
1(45)-1	1	45°	208.9	223.8	104.5	111.9	67,160
1(45)-2	1	45°	223.8	238.7	111.9	119.4	46,822
1(45)-3	1	45°	238.7	253.7	119.4	126.9	25,276
1(90)-1	1	90°	282.9	298.5	141.5	149.3	63,105
1(90)-2	1	90°	283.5	298.4	141.8	149.2	88,655
1(90)-3	1	90°	311.8	334.1	155.9	167.0	28,730



Table 5. Constants of Eq.s (12)-(15) computed from the low-cycle fatigue tests.

σ'_f (MPa)	b	ε'_f	c	κ_t (MJ/m ³)	α_t	ΔW_{t0} (MJ/m ³)
1183.7	-0.0545	0.4697	-0.6059	2165.37	-0.6854	0.7049

Declaration of interests

The authors declare that they have no known competing financial interests or personal relationships that could have appeared to influence the work reported in this paper.

The authors declare the following financial interests/personal relationships which may be considered as potential competing interests: